# Non-smooth 3D Modeling of a Snake Robot with Frictional Unilateral Constraints

Aksel Andreas Transeth*, Remco I. Leine†, Christoph Glocker†, and Kristin Y. Pettersen*
*Department of Engineering Cybernetics, NTNU, NO-7491 Trondheim, Norway
E-mail: Aksel.Andreas.Transeth@itk.ntnu.no, Kristin.Y.Pettersen@itk.ntnu.no
† IMES–Center of Mechanics, ETH Zürich, CH-8092 Zürich, Switzerland
E-mail: Remco.Leine@imes.mavt.ethz.ch, Christoph.Glocker@imes.mavt.ethz.ch

***Abstract*— A *non-smooth* 3D mathematical model of the dynamics of a snake robot (without wheels) is developed in this paper. The model is based on the framework of non-smooth dynamics and convex analysis which allows us to easily incorporate unilateral contact forces and friction forces based on Coulomb's law of dry friction. Impact and stick-slip transitions are modeled as instantaneous. A numerical integrator on impulse-velocity level, the time-stepping method, is used for simulation, which helps avoid an explicit switch between equations of motion during simulation. Numerical results are presented for a snake robot with 26 degrees of freedom and 22 possible contact points along its body. Simulation results of the snake motion pattern 'lateral undulation' are shown.**

***Index Terms*— Non-smooth dynamics, 3D snake robot**

## I. Introduction

Wheeled mechanisms constitute the backbone of most ground-based means of transportation. Unfortunately, rough terrain makes it hard, if not impossible, for such mechanisms to move. To be able to move in various terrains, such as going through narrow passages and climb on rough ground, the high-mobility property of snakes is recreated in robots that look and move like snakes. Snake robots most often have a high number of degrees of freedom (DOF) and they are able to move forward without using active wheels or legs.

Ever since Hirose [1] built the first working snake robot in 1972, mathematical models of the dynamics of such robots have been developed. Usually, these models only consider planar motion. The first 3D model of the dynamics of a snake robot was published in 2004 [2]. The models of the dynamics for both 2D and 3D have been developed from the Newton-Euler equations [2], [3], or the Lagrange formulation [4].

The purpose of this paper is to develop and simulate a novel model of a snake robot based on the framework of non-smooth dynamics and convex analysis. The description of the model and the method for numerical integration are presented in this paper in such a way that people who are new to the field of non-smooth dynamics can use this paper as an introduction to non-smooth modeling of robot manipulators with impacts and friction.

On a flat surface, the ability of the snake robot to move forward is dependent on the friction between the ground surface and the body of the snake robot. Hence, the unilateral contact forces and the friction forces are important parts of the mathematical model of a snake robot. The friction forces have usually been based on a Coulomb or viscous-like friction model [4], [5], and the Coulomb friction has most often been modeled using the sign-function [2], [5]. The unilateral contact forces have been modeled as a mass-spring-damper system in [3]. However, when running simulations, direct implementations or approximations of the sign-function can lead to an erroneous description of sticking contacts or very stiff differential equations. Also, a mass-spring-damper model introduces a very stiff spring that leads to stiff differential equations.

In this paper, the first non-smooth 3D mathematical model of a snake robot is developed. Set-valued force laws for the constitutive description of the unilateral contact forces and the friction forces in a three-dimensional setting are described in the framework of non-smooth dynamics and convex analysis [6]–[8]. Stick-slip transitions (based on a set-valued Coulomb friction law) and impacts with the ground are modeled as instantaneous transitions. The dynamics is described by an equality of measures, which includes the Newton-Euler equations for the non-impulsive part of the motion as well as the impact equations. A particular choice of coordinates results in an effective way of writing the system equations. Contact forces and impulses are included as Lagrangian multipliers in the equality of measures. The set-valuedness of the force laws allows us to write each constitutive law with a single equation and avoids explicit switching between equations. A discretization of the equality of measures gives the so-called time-stepping method (see [8] and references therein) which we use for numerical simulation.

In the following, the various modeling steps will be discussed for the development of the 3D mathematical model of a snake robot with unilateral frictional contact. The choice of coordinates and reference frames, as well as the contact constraints expressed in gap functions are given in Section II. Section III shows how to obtain expressions for the relative velocities, needed to find the contact and friction forces, from the gap functions. Section IV describes the non-smooth dynamics of the snake robot and Section V discusses the control of the joint angles. Section VI presents the time-stepping method while Section VII contains the simulation results. Conclusions and suggestions for further research are presented in Section VIII.

## II. Kinematics

The kinematics describes the geometrical aspect of motion. From the geometry, we develop *gap functions* for ground contact detection. These functions are also needed for calculating the directions of the contact forces.

This section will first give an overview of the coordinates used to describe the position and orientation of the snake robot. Subsequently, the gap functions will be presented.

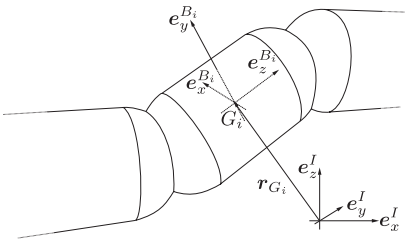


Fig. 1. Reference frames.

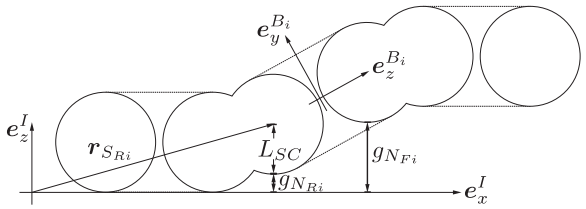


Fig. 2. Surfaces (solid-drawn circles) on snake robot that constitute the contact between the robot and the ground.

### A. Coordinates and Reference Frames

The snake robot consists of $n$ cylindrical links that are connected by $n-1$ cardan joints, each having two degrees of freedom (DOF). The distance $L_i$ between two adjacent cardan joints equals the length of link $i$, and the radius of each link is $L_{SC}$. We denote the earth-fixed coordinate frame $I = \left(O, \boldsymbol{e}_x^I, \boldsymbol{e}_y^I, \boldsymbol{e}_x^I\right)$, see Fig. 1, as an approximation to an inertial frame where its centre $O$ is fixed to the ground surface and the $\boldsymbol{e}_z^I$-axis is pointing in the opposite direction of the acceleration of gravity vector $\boldsymbol{g}$.

The position and orientation of link $i$ are described by the *non-minimal absolute* coordinates

$$\boldsymbol{q}_i = \begin{bmatrix} {}_I\boldsymbol{r}_{G_i} \\ \boldsymbol{p}_i \end{bmatrix} \in \mathbb{R}^7, \tag{1}$$

where ${}_I\boldsymbol{r}_{G_i} \in \mathbb{R}^3$ is the position of the centre of gravity of link $i$ and the vector $\boldsymbol{p}_i = \begin{bmatrix} e_{i_0} & \boldsymbol{e}_i^{\mathrm{T}} \end{bmatrix}^{\mathrm{T}}$, where $\boldsymbol{e}_i^{\mathrm{T}} = \begin{bmatrix} e_{i_1} & e_{i_2} & e_{i_3} \end{bmatrix}$, contains the four Euler parameters used to describe the rotation. The Euler parameters form a unit quaternion vector with the constraint $\boldsymbol{p}_i^{\mathrm{T}}\boldsymbol{p}_i = 1$. The coordinates are *non-minimal* because each link is described with 6 coordinates, and *absolute* because the position and orientation of link $i$ is given directly relative to frame $I$. The velocity of link $i$ is given by

$$\boldsymbol{u}_i = \begin{bmatrix} {}_I\boldsymbol{v}_{G_i} \\ {}_{B_i}\boldsymbol{\omega}_{IB_i} \end{bmatrix} \in \mathbb{R}^6 \tag{2}$$

where ${}_I\boldsymbol{v}_{G_i}$ is the translational velocity of the CG of link $i$ which is ${}_I\boldsymbol{v}_{G_i} = {}_I\dot{\boldsymbol{r}}_{G_i}$ when it exists (i.e. for impact free motion). Moreover, ${}_{B_i}\boldsymbol{\omega}_{IB_i}$ is the angular velocity of frame $B_i$ relative to frame $I$, given in frame $B_i$. The transformation ${}_I\boldsymbol{r} = \mathbf{R}_{B_i\,B_i}^I\boldsymbol{r}$ can be performed with the rotation matrix $\mathbf{R}_{B_i}^I = \mathbf{H}_i\bar{\mathbf{H}}_i$ where

$$\mathbf{H}_i = \begin{bmatrix} -\boldsymbol{e}_i & \tilde{\boldsymbol{e}}_i + e_{i_0}\mathbf{I} \end{bmatrix}, \; \bar{\mathbf{H}}_i = \begin{bmatrix} -\boldsymbol{e}_i & -\tilde{\boldsymbol{e}}_i + e_{i_0}\mathbf{I} \end{bmatrix}, \tag{3}$$

and the superscript $\tilde{}$ denotes the skew-symmetric form of $\boldsymbol{e}$. The matrices $\mathbf{H}_i$ and $\bar{\mathbf{H}}_i$ are also used in the mapping from $\boldsymbol{u}$ to $\dot{\boldsymbol{q}}$ (when they exist) in Section VI-A. The time-derivative of the rotation matrix is found from [9] as

$$\dot{\mathbf{R}}_{B_i}^I = \mathbf{R}_{B_i\,B_i}^I\tilde{\boldsymbol{\omega}}_{IB_i}. \tag{4}$$

The coordinates (positions and orientation) and velocities of all links are gathered in the vectors $\boldsymbol{q} = \begin{bmatrix} \boldsymbol{q}_1^{\mathrm{T}} & \cdots & \boldsymbol{q}_n^{\mathrm{T}} \end{bmatrix}^{\mathrm{T}}$ and $\boldsymbol{u} = \begin{bmatrix} \boldsymbol{u}_1^{\mathrm{T}} & \cdots & \boldsymbol{u}_n^{\mathrm{T}} \end{bmatrix}^{\mathrm{T}}$.

### B. Gap Functions for Unilateral Constraints

The gap functions for the unilateral constraints (i.e. the floor) give the minimal distance between the floor and the front and rear part of each link. The contact surfaces between a link and the ground are modeled as two spheres at the ends of the link as illustrated for a three-link robot in Fig. 2.

We denote the distance between the centre of the two spheres that belong to link $i$ by $2L_{GS_i}$ and the radius of the spheres by $L_{SC}$. The position of the centre of the front and rear spheres are denoted by $\boldsymbol{r}_{S_{Fi}}$ and $\boldsymbol{r}_{S_{Ri}}$, respectively. The shortest distance between the ground and the points on the front and rear spheres closest to the ground are denoted by $g_{N_{Fi}}$ and $g_{N_{Ri}}$, respectively. The distances are found from

$$g_{N_{Fi}} = \left(\boldsymbol{r}_{S_{Fi}}\right)^{\mathrm{T}}\boldsymbol{e}_z^I - L_{SC}, \; g_{N_{Ri}} = \left(\boldsymbol{r}_{S_{Ri}}\right)^{\mathrm{T}}\boldsymbol{e}_z^I - L_{SC}, \tag{5}$$

where $\boldsymbol{r}_{S_{Fi}} = \boldsymbol{r}_{G_i} + L_{GS_i}\boldsymbol{e}_z^{B_i}$, $\boldsymbol{r}_{S_{Ri}} = \boldsymbol{r}_{G_i} - L_{GS_i}\boldsymbol{e}_z^{B_i}$.

The gap functions are gathered in the vector

$$\boldsymbol{g}_N = \begin{bmatrix} g_{N_{F1}} & \cdots & g_{N_{Fn}} & g_{N_{R1}} & \cdots & g_{N_{Rn}} \end{bmatrix}^{\mathrm{T}}. \tag{6}$$

### C. Gap Functions for Bilateral Constraints

Each 2 DOF cardan joint introduces four bilateral constraints, which will be described by gap functions.

To find the translational'gap' in the joints, we need to relate the position of the joint between link $i$ and $i+1$ to both links. Let the position of the joint between link $i$ and $i+1$ be written as ${}_I\boldsymbol{r}_{J_{Fi}} = {}_I\boldsymbol{r}_{G_i} + \frac{1}{2}L_i\,{}_I\boldsymbol{e}_z^{B_i}$, ${}_I\boldsymbol{r}_{J_{Ri+1}} = {}_I\boldsymbol{r}_{G_{i+1}} - \frac{1}{2}L_i\,{}_I\boldsymbol{e}_z^{B_{i+1}}$. The gap functions can now be found from

$$g_{J_{\chi i}} = \left({}_I\boldsymbol{r}_{J_{Fi}} - {}_I\boldsymbol{r}_{J_{Ri+1}}\right)^{\mathrm{T}}{}_I\boldsymbol{e}_\chi^I, \tag{7}$$

for $i = 1, \ldots, n-1$, and $\chi = x, y, z$. Hence,

$$\begin{aligned} g_{J_{\chi i}} = &\left({}_I\boldsymbol{r}_{G_i} - {}_I\boldsymbol{r}_{G_{i+1}}\right)^{\mathrm{T}}{}_I\boldsymbol{e}_\chi^I \\ &+ \frac{1}{2}\left(L_i\mathbf{R}_{B_i\,B_i}^I\boldsymbol{e}_z^{B_i} + L_{i+1}\mathbf{R}_{B_{i+1}\,B_{i+1}}^I\boldsymbol{e}_z^{B_{i+1}}\right)^{\mathrm{T}}{}_I\boldsymbol{e}_\chi^I \end{aligned} \tag{8}$$

for $i = 1, \ldots, n-1$.

The next gap function provides the 'gap' in rotation around the axis that a cardan joint is not able to rotate around. Let $\boldsymbol{e}_y^{B_i}$ and $\boldsymbol{e}_x^{B_{i+1}}$ be the axes of rotation for the cardan joint between link $i$ and link $i+1$, then $\left(\boldsymbol{e}_y^{B_i}\right)^{\mathrm{T}}\boldsymbol{e}_x^{B_{i+1}} = 0$. Hence, a measure for the rotational 'gap' can be defined from the equality above as the gap function

$$g_{Ji_\phi} = \left(\mathbf{R}_{B_i\,B_i}^I\boldsymbol{e}_y^{B_i}\right)^{\mathrm{T}}\left(\mathbf{R}_{B_{i+1}\,B_{i+1}}^I\boldsymbol{e}_x^{B_{i+1}}\right) \tag{9}$$

## III. Contact Constraints on Velocity Level

In this section we calculate the relative velocities between the snake robot and the ground from the gap functions. The relative velocities are needed to set up the set-valued contact forces for the closed contacts [10].

### A. Unilateral Contact - Ground Contact

The contact between the snake robot and the ground involves (vertical) normal forces, which guarantee the unilateriality of the contact, and (horizontal) tangential contact forces, which are due to friction and are dependent on the normal contact forces and the relative sliding velocities.

*1) Relative Velocities Along $\boldsymbol{e}_z^I$:* The relative velocities between the front and rear part of link $i$ and the ground along the $\boldsymbol{e}_z^I$-axis are defined as $\gamma_{N_{Fi}} := \dot{g}_{N_{Fi}}$ and $\gamma_{N_{Ri}} := \dot{g}_{N_{Ri}}$, respectively (if they exist) [10]. Before calculating the relative velocities, we need to consider the speed of the contact points between the link and the ground. Let $C_{Fi}$ be the body-fixed point on the front sphere which is momentarily closest to the ground. The velocity of the point $\boldsymbol{r}_{C_{Fi}} = \boldsymbol{r}_{G_i} + \boldsymbol{r}_{G_{Fi}S_{Fi}} - L_{SC}\boldsymbol{e}_z^I$ is found using (4) as

$$ {}_I\boldsymbol{v}_{C_{Fi}} = {}_I\boldsymbol{v}_{G_i} - \mathbf{R}^I_{B_i\ B_i}\tilde{\boldsymbol{r}}_{G_iS_{Fi}\ B_i}\boldsymbol{\omega}_{IB_i}. \tag{10} $$

Now, the relative velocities for the front and rear part of link $i$ can be found as

$$ \gamma_{N_{Qi}} = ({}_I\boldsymbol{e}_z^I)^{\mathrm{T}}\,{}_I\boldsymbol{v}_{C_{Qi}} \Longrightarrow \gamma_{N_{Qi}} = (\boldsymbol{w}_{N_{Qi}})^{\mathrm{T}}\boldsymbol{u}_i, \tag{11} $$

where

$$ \boldsymbol{w}_{N_{Qi}} = \begin{bmatrix} ({}_I\boldsymbol{e}_z^I)^{\mathrm{T}} & -({}_I\boldsymbol{e}_z^I)^{\mathrm{T}}\mathbf{R}^I_{B_i\ B_i}\tilde{\boldsymbol{r}}^{B_i}_{G_iS_{Qi}} \end{bmatrix}^{\mathrm{T}}, \tag{12} $$

for $Q = F, R$ with $\boldsymbol{r}_{G_iS_{Fi}} = L_{GS_i}\boldsymbol{e}_z^{B_i}$ and $\boldsymbol{r}_{G_iS_{Ri}} = -L_{GS_i}\boldsymbol{e}_z^{B_i}$. The motivation to use the form (11) is that $\boldsymbol{w}_{N_{Qi}}$ gives the generalised direction of the contact force between the ground and the front and rear part on link $i$.

A vector gathering all $\gamma_{N_{Fi}}$ and $\gamma_{N_{Ri}}$ is

$$ \boldsymbol{\gamma}_N = \mathbf{W}_N^{\mathrm{T}}\boldsymbol{u} \tag{13} $$

where $\boldsymbol{\gamma}_N = \begin{bmatrix}\gamma_{N_{F1}} & \cdots & \gamma_{N_{Fn}} & \gamma_{N_{R1}} & \cdots & \gamma_{N_{Rn}}\end{bmatrix}^{\mathrm{T}}$, $\mathbf{W}_N = \begin{bmatrix}\mathbf{W}_{N_F} & \mathbf{W}_{N_R}\end{bmatrix} \in \mathbb{R}^{6n\times 2n}$, and

$$ \mathbf{W}_{N_Q} = \begin{bmatrix} \boldsymbol{w}_{N_{Q1}} & \mathbf{0}_{6\times 1} & \cdots & \mathbf{0}_{6\times 1} \\ \mathbf{0}_{6\times 1} & \ddots & & \vdots \\ \vdots & & \ddots & \mathbf{0}_{6\times 1} \\ \mathbf{0}_{6\times 1} & \cdots & \mathbf{0}_{6\times 1} & \boldsymbol{w}_{N_{Qn}} \end{bmatrix}, \tag{14} $$

for $Q = F, R$.

*2) Tangential Relative Velocities:* The friction forces between a link and the ground depend on the relative velocities in the $(\boldsymbol{e}_x^I, \boldsymbol{e}_y^I)$-plane. First, the relative velocities between the front part of link $i$ and the ground along the $\boldsymbol{e}_x^I$- and $\boldsymbol{e}_y^I$-axis, $\gamma'_{T_{Fxi}}$ and $\gamma'_{T_{Fyi}}$, will be deducted. Subsequently, the relative velocities for the front part of link $i$ along the direction of the link $\gamma_{T_{Fxi}}$, and transversal to the link $\gamma_{T_{Fyi}}$, will be deducted from $\gamma'_{T_{Fxi}}$ and $\gamma'_{T_{Fyi}}$. The same type of notation applies for the rear part of link $i$: $\gamma'_{T_{Rxi}}$, $\gamma'_{T_{Ryi}}$, $\gamma_{T_{Rxi}}$, and $\gamma_{T_{Ryi}}$. The tangential relative velocities are found much in the same way as for $\gamma_{N_{Fi}}$ and $\gamma_{N_{Ri}}$. Hence, by looking at (11), we see that the relative velocities of the contact points on the front part of the link can be found as

$$ \gamma'_{T_{F\zeta i}} = ({}_I\boldsymbol{e}_\zeta^I)^{\mathrm{T}}\,{}_I\boldsymbol{v}_{C_{Fi}} \Longrightarrow \gamma'_{T_{F\zeta i}} = (\boldsymbol{w}'_{T_{F\zeta i}})^{\mathrm{T}}\boldsymbol{u}_i \tag{15} $$

for $\zeta = x, y$, where

$$ \boldsymbol{w}'_{T_{F\zeta i}} = \begin{bmatrix} ({}_I\boldsymbol{e}_\zeta^I)^{\mathrm{T}} & -({}_I\boldsymbol{e}_\zeta^I)^{\mathrm{T}}\mathbf{R}^I_{B_i\ B_i}\tilde{\boldsymbol{e}}_z^{B_i}L_{GS_i} \end{bmatrix}^{\mathrm{T}}. \tag{16} $$

The relative velocities between the rear part of the link and the ground are found by exchanging ${}_I\boldsymbol{v}_{C_{Fi}}$ with ${}_I\boldsymbol{v}_{C_{Ri}}$ in (15):

$$ \gamma'_{T_{R\zeta i}} = ({}_I\boldsymbol{e}_\zeta^I)^{\mathrm{T}}\,{}_I\boldsymbol{v}_{C_{Ri}} \Longrightarrow \gamma'_{T_{R\zeta i}} = (\boldsymbol{w}'_{T_{R\zeta i}})^{\mathrm{T}}\boldsymbol{u}_i \tag{17} $$

for $\zeta = x, y$, where

$$ \boldsymbol{w}'_{T_{R\zeta i}} = \begin{bmatrix} ({}_I\boldsymbol{e}_\zeta^I)^{\mathrm{T}} & ({}_I\boldsymbol{e}_\zeta^I)^{\mathrm{T}}\mathbf{R}^I_{B_i\ B_i}\tilde{\boldsymbol{e}}_z^{B_i}L_{GS_i} \end{bmatrix}^{\mathrm{T}}. \tag{18} $$

The tangential relative velocities for the front and rear part of the link are combined in vectors:

$$ \boldsymbol{\gamma}'_{T_{Qi}} = \mathbf{W}'^{\mathrm{T}}_{T_{Qi}}\boldsymbol{u}_i \tag{19} $$

for $Q = F, R$, where $\boldsymbol{\gamma}'_{T_{Qi}} = \begin{bmatrix}\gamma'_{T_{Qxi}} & \gamma'_{T_{Qyi}}\end{bmatrix}^{\mathrm{T}}$ and

$$ \mathbf{W}'_{T_{Qi}} = \begin{bmatrix}\boldsymbol{w}'_{T_{Qxi}} & \boldsymbol{w}'_{T_{Qyi}}\end{bmatrix}. \tag{20} $$

Until now, the relative velocities have been given in the directions along the $\boldsymbol{e}_x^I$ and $\boldsymbol{e}_y^I$ axes. In order to calculate the friction forces longitudinal and transversal to a link, we need to know the corresponding relative velocities in these directions in the $(\boldsymbol{e}_x^I, \boldsymbol{e}_y^I)$-plane. To calculate these velocities we introduce for each link a frame $\Pi_i$ with axes $(\boldsymbol{e}_x^{\Pi_i}, \boldsymbol{e}_y^{\Pi_i}, \boldsymbol{e}_z^{\Pi_i})$, where ${}_I\boldsymbol{e}_z^{\Pi_i} = {}_I\boldsymbol{e}_z^I$, and

$$ {}_I\boldsymbol{e}_x^{\Pi_i} = \frac{\mathbf{A}_{xy}\,{}_I\boldsymbol{e}_z^{B_i}}{\|\mathbf{A}_{xy}\,{}_I\boldsymbol{e}_z^{B_i}\|}, \quad {}_I\boldsymbol{e}_y^{\Pi_i} = \frac{{}_I\boldsymbol{e}_z^I \times {}_I\boldsymbol{e}_x^{\Pi_i}}{\|{}_I\boldsymbol{e}_z^I \times {}_I\boldsymbol{e}_x^{\Pi_i}\|} \tag{21} $$

where $\mathbf{A}_{xy} = \mathrm{diag}([1,\ 1,\ 0])$. Hence, $\mathbf{R}^I_{\Pi_i} = [{}_I\boldsymbol{e}_x^{\Pi_i}\ {}_I\boldsymbol{e}_y^{\Pi_i}\ {}_I\boldsymbol{e}_z^{\Pi_i}]$. Since only the motion in the $(\boldsymbol{e}_x^I, \boldsymbol{e}_y^I)$-plane is of interest, we define

$$ \bar{\mathbf{R}}^I_{\Pi_i} = \mathbf{D}^{\mathrm{T}}\mathbf{R}^I_{\Pi_i}\mathbf{D}, \quad \mathbf{D} = \begin{bmatrix}1 & 0 & 0\\ 0 & 1 & 0\end{bmatrix}^{\mathrm{T}} \tag{22} $$

Since we now have that $\boldsymbol{\gamma}'_{T_{Qi}} = \bar{\mathbf{R}}^I_{\Pi_i}\boldsymbol{\gamma}_{T_{Qi}}$, $Q = F, R$, the relative velocity between the floor and the front part of link $i$, with respect to frame $\Pi_i$, can be found from (19) as

$$ \boldsymbol{\gamma}_{T_{Qi}} = \mathbf{W}^{\mathrm{T}}_{T_{Qi}}\boldsymbol{u}_i, \tag{23} $$

where $\boldsymbol{\gamma}_{T_{Qi}} = \begin{bmatrix}\gamma_{T_{Qxi}} & \gamma_{T_{Qyi}}\end{bmatrix}^{\mathrm{T}}$, $\mathbf{W}_{T_{Qi}} = \mathbf{W}'_{T_{Qi}}\bar{\mathbf{R}}^I_{\Pi_i}$, for $Q = F, R$.

A vector that gathers all $\boldsymbol{\gamma}_{T_{Fi}}$ and $\boldsymbol{\gamma}_{T_{Ri}}$ is found from

$$ \boldsymbol{\gamma}_T = \mathbf{W}_T^{\mathrm{T}}\boldsymbol{u} \tag{24} $$

where $\boldsymbol{\gamma}_T = \begin{bmatrix}\boldsymbol{\gamma}^{\mathrm{T}}_{T_{F1}} & \cdots & \boldsymbol{\gamma}^{\mathrm{T}}_{T_{Fn}} & \boldsymbol{\gamma}^{\mathrm{T}}_{T_{R1}} & \cdots & \boldsymbol{\gamma}^{\mathrm{T}}_{T_{Rn}}\end{bmatrix}^{\mathrm{T}}$, $\mathbf{W}_T = \begin{bmatrix}\mathbf{W}_{T_F} & \mathbf{W}_{T_R}\end{bmatrix} \in \mathbb{R}^{6n\times 4n}$, and $\mathbf{W}_{T_F}$, $\mathbf{W}_{T_R}$ are found similarly to (14) by replacing the zero-vectors with $\mathbf{0}_{6\times 2}$ and replacing the vectors $\boldsymbol{w}_{N_{Fi}}$, $\boldsymbol{w}_{N_{Ri}}$ with the matrices $\mathbf{W}_{T_{Fi}}$, $\mathbf{W}_{T_{Ri}}$, respectively.

### B. Bilateral Constraints - Joints

The relative velocities of gaps introduced by the bilateral constraints will be calculated in the following from the gap functions (8) and (9) to find the joint constraint forces.

The relative velocities for the translational gap between link $i$ and link $i+1$ are defined as $\gamma_{Ji_\chi} := \dot{g}_{J_{\chi i}}$ for $i = 1, \ldots, n-1$ where $\chi = x, y, z$. By employing (8), we find that

$$ \gamma_{J_{\chi i}} = \boldsymbol{w}^{\mathrm{T}}_{J_{\chi i}}\begin{bmatrix}\boldsymbol{u}_i \\ \boldsymbol{u}_{i+1}\end{bmatrix}, \tag{25} $$

where

$$\boldsymbol{w}_{J_{\chi i}} = \begin{bmatrix} ({}_I\boldsymbol{e}_\chi^I) \\ -\left(({}_I\boldsymbol{e}_\chi^I)^{\mathrm{T}} \frac{L_i}{2} \mathbf{R}^I_{B_i\ B_i} \tilde{\boldsymbol{e}}_z^{B_i}\right)^{\mathrm{T}} \\ -({}_I\boldsymbol{e}_\chi^I) \\ -\left(({}_I\boldsymbol{e}_\chi^I)^{\mathrm{T}} \frac{L_{i+1}}{2} \mathbf{R}^I_{B_{i+1}\ B_{i+1}} \tilde{\boldsymbol{e}}_z^{B_{i+1}}\right)^{\mathrm{T}} \end{bmatrix}. \tag{26}$$

The relative velocity for the rotational gap is defined as $\gamma_{J_{\phi i}} := \dot{g}_{J_{\phi i}}$ for $i = 1, \ldots, n-1$. Hence,

$$\gamma_{J_{\phi i}} = \boldsymbol{w}_{J_{\phi i}}^{\mathrm{T}} \begin{bmatrix} \boldsymbol{u}_i \\ \boldsymbol{u}_{i+1} \end{bmatrix}, \tag{27}$$

where

$$\boldsymbol{w}_{J_{\phi i}} = \begin{bmatrix} \mathbf{0}_{3\times 1} \\ -\left(\mathbf{R}^I_{B_i\ B_i} \tilde{\boldsymbol{e}}_y^{B_i}\right)^{\mathrm{T}} \left(\mathbf{R}^I_{B_{i+1}\ B_{i+1}} \boldsymbol{e}_x^{B_{i+1}}\right) \\ \mathbf{0}_{3\times 1} \\ -\left(\mathbf{R}^I_{B_{i+1}\ B_{i+1}} \tilde{\boldsymbol{e}}_x^{B_{i+1}}\right)^{\mathrm{T}} \left(\mathbf{R}^I_{B_i\ B_i} \boldsymbol{e}_y^{B_i}\right) \end{bmatrix}. \tag{28}$$

Let $\boldsymbol{\gamma}_{J_i} = \begin{bmatrix} \gamma_{J_{xi}} & \gamma_{J_{yi}} & \gamma_{J_{zi}} & \gamma_{J_{\chi i}} \end{bmatrix}^{\mathrm{T}}$, then we can gather all the relative velocities concerned with the bilateral constraints in one vector

$$\boldsymbol{\gamma}_J = \mathbf{W}_J^{\mathrm{T}} \boldsymbol{u}, \tag{29}$$

where $\boldsymbol{\gamma}_J = \begin{bmatrix} \boldsymbol{\gamma}_{J_1}^{\mathrm{T}} & \cdots & \boldsymbol{\gamma}_{J_{n-1}}^{\mathrm{T}} \end{bmatrix}^{\mathrm{T}}$,

$$\mathbf{W}_J = \begin{bmatrix} \mathbf{W}_{J1}^{\mathrm{T}} & \mathbf{0}_{4\times 6} & \cdots & \mathbf{0}_{4\times 6} \\ \mathbf{0}_{4\times 6} & \mathbf{W}_{J2}^{\mathrm{T}} & & \vdots \\ \vdots & & \ddots & \mathbf{0}_{4\times 6} \\ \mathbf{0}_{4\times 6} & \cdots & \mathbf{0}_{4\times 6} & \mathbf{W}_{Jn-1}^{\mathrm{T}} \end{bmatrix}^{\mathrm{T}} \in \mathbb{R}^{6n\times 4(n-1)}, \tag{30}$$

and $\mathbf{W}_{Ji} = \begin{bmatrix} \boldsymbol{w}_{Ji_x} & \boldsymbol{w}_{Ji_y} & \boldsymbol{w}_{Ji_z} & \boldsymbol{w}_{Ji_\phi} \end{bmatrix} \in \mathbb{R}^{12\times 4}$ for $i = 1, \ldots, n-1$.

## IV. Non-smooth Dynamics

The starting point for describing the dynamics of the snake robot is the *equality of measures* as introduced in [11]. The equality of measures includes the equations of motion for impact free motion as well as the impact equations. The impact equations give rise to impulsive behaviour [12].

### A. The Equality of Measures

The equality of measures describes the dynamics of the snake robot within the context of non-smooth dynamics. Velocity jumps, usually associated with impacts, are modeled to occur instantaneously. By considering the generalised velocity to be a function $t \mapsto \boldsymbol{u}(t)$ of locally bounded variation on a time-interval $I = [t_A, t_E]$ [11], the function $\boldsymbol{u}(t)$ admits a right $\boldsymbol{u}^+$ and left $\boldsymbol{u}^-$ limit for all $t \in I$, and its time-derivative $\dot{\boldsymbol{u}}$ exists for almost all $t \in I$. To be able to obtain $\boldsymbol{u}$ from integration we need to use the differential measure $\mathrm{d}\boldsymbol{u}$ where it is assumed that the measure can be decomposed into

$$\mathrm{d}\boldsymbol{u} = \dot{\boldsymbol{u}}\mathrm{d}t + \left(\boldsymbol{u}^+ - \boldsymbol{u}^-\right)\mathrm{d}\eta \tag{31}$$

where $\mathrm{d}t$ denotes the Lebesgue measure and $\mathrm{d}\eta$ denotes the atomic measure where $\int_{\{t_1\}} \mathrm{d}\eta = 1$. The total increment of $\boldsymbol{u}$ over a compact subinterval $[t_1, t_2]$ of $I$, is written as

$$\int_{[t_1,t_2]} \mathrm{d}\boldsymbol{u} = \boldsymbol{u}^+(t_2) - \boldsymbol{u}^-(t_1), \tag{32}$$

and is due to a continuous change stemming from $\dot{\boldsymbol{u}}$ as well as possible discontinuities in $\boldsymbol{u}$ within the time-interval $[t_1, t_2]$. Equation (32) is also valid when the time-interval reduces to a singleton $\{t_1\}$, and if a velocity jump occurs for $t = t_1$ then (32) gives a nonzero result.

From the notation above, the Newton-Euler equations as equality of measures can be written in a general form as

$$\mathbf{M}(\boldsymbol{q}, t)\,\mathrm{d}\boldsymbol{u} - \boldsymbol{h}(\boldsymbol{q}, \boldsymbol{u}, t)\,\mathrm{d}t - \mathrm{d}\boldsymbol{R} = \boldsymbol{\tau}_C \mathrm{d}t \tag{33}$$

where the mass matrix $\mathbf{M}(\boldsymbol{q}, t)$, the vector of smooth forces $\boldsymbol{h}(\boldsymbol{q}, \boldsymbol{u}, t)$, the force measure of possibly atomic impact impulsions $\mathrm{d}\boldsymbol{R}$, and the vector of applied torques $\boldsymbol{\tau}_C$ will be described in the following.

For our choice of coordinates, the mass matrix is *diagonal* and constant

$$\mathbf{M}(\boldsymbol{q}, t) = \mathbf{M} = \begin{bmatrix} \mathbf{M}_1 & & \mathbf{0} \\ & \ddots & \\ \mathbf{0} & & \mathbf{M}_n \end{bmatrix} \in \mathbb{R}^{6n\times 6n} \tag{34}$$

where

$$\mathbf{M}_i = \begin{bmatrix} m_i \mathbf{I}_{3\times 3} & \mathbf{0}_{3\times 3} \\ \mathbf{0}_{3\times 3} & {}_{B_i}\boldsymbol{\Theta}_{G_i} \end{bmatrix}, \tag{35}$$

with ${}_{B_i}\boldsymbol{\Theta}_{G_i} = \mathrm{diag}\left(\begin{bmatrix} \Theta_{1i} & \Theta_{1i} & \Theta_{3i} \end{bmatrix}\right)$, $m_i$ is the mass of link $i$, and $\Theta_{1i}$ and $\Theta_{3i}$ are its moments of inertia. The smooth forces, here consisting of gravity and gyroscopic accelerations, are described by $\boldsymbol{h}(\boldsymbol{q}, \boldsymbol{u}, t) = \boldsymbol{h}(\boldsymbol{u}) = \begin{bmatrix} \boldsymbol{h}_1^{\mathrm{T}}(\boldsymbol{u}_1) & \cdots & \boldsymbol{h}_n^{\mathrm{T}}(\boldsymbol{u}_n) \end{bmatrix}^{\mathrm{T}} \in \mathbb{R}^{6n}$, where $\boldsymbol{h}_i(\boldsymbol{u}_i) = \begin{bmatrix} 0 & 0 & -m_i g & -({}_{B_i}\tilde{\boldsymbol{\omega}}_{IB_i\ B_i}\boldsymbol{\Theta}_{G_i\ B_i}\boldsymbol{\omega}_{IB_i}) \end{bmatrix}^{\mathrm{T}}$.

The force measure $\mathrm{d}\boldsymbol{R}$ accounts for all the contact forces and impulses. The contact efforts that constitute $\mathrm{d}\boldsymbol{R}$ are found from the force-laws given in Section IV-B. Let $\mathcal{I}$ be the set of all active contacts with the ground

$$\mathcal{I}(t) = \{a \mid g_{N_a}(\boldsymbol{q}(t)) = 0\} \subseteq \{1, 2, \ldots, 2n\}, \tag{36}$$

where $g_{N_a}$ is the $a$-th element of the vector $\boldsymbol{g}_N$ in (6). Now, the force measure is written as

$$\begin{aligned} \mathrm{d}\boldsymbol{R} = &\sum_{a\in\mathcal{I}} ((\mathbf{W}_N)_a\,\mathrm{d}\Lambda_{N_a}) + \mathbf{W}_J\,\mathrm{d}\boldsymbol{\Lambda}_J \\ &+ \sum_{a\in\mathcal{I}} \left((\mathbf{W}_T)_{2a-1}\,\mathrm{d}\Lambda_{T_{xa}} + (\mathbf{W}_T)_{2a}\,\mathrm{d}\Lambda_{T_{ya}}\right) \end{aligned} \tag{37}$$

where $\mathrm{d}\Lambda_{N_a}$ is the normal contact impulse measure between the ground and a link, $\mathrm{d}\Lambda_{T_{xa}}$ and $\mathrm{d}\Lambda_{T_{ya}}$ are the tangential contact impulse measures (friction) between the floor and a link, longitudinal and transversal to the link, respectively, $\mathrm{d}\boldsymbol{\Lambda}_J$ is the contact impulse measure due to the bilateral constraints in the joints (these constraints are always active), and the lower-case subscripts on the $\mathbf{W}$-matrices indicate which column of the matrix is used. The contact impulse measures can be decomposed in the same way as for $\mathrm{d}\boldsymbol{u}$. Let us take the normal contact impulse measure as an example. The measure can be written as

$$\mathrm{d}\Lambda_{N_a} = \lambda_{N_a}\mathrm{d}t + P_{N_a}\mathrm{d}\eta \tag{38}$$

where $\lambda_{N_a}$ is the Lebesgue-measurable force and $P_{N_a}$ is the purely atomic impact impulse. The same decomposition can also be performed for the three other impulse measures.

The control torques $\boldsymbol{\tau}_C$ are described in Section IV-C below.

### B. Constitutive Laws for the Contact Forces

In this section, we will introduce set-valued force laws for normal contact and Coulomb friction. These laws will all be formulated on velocity level using the relative contact velocities $\gamma$ given by (13) and (24). Subsequently, the set-valued force laws are formulated as equalities in Section IV-B.3 using the so-called 'proximal point function' in order to include the force laws in the numerical simulation [8].

*1) Normal Contact Force:* The normal contact between a link and the floor is described by the unilateral constraint

$$g_N \geq 0,\ \lambda_N \geq 0, \quad g_N \lambda_N = 0, \tag{39}$$

which is known as Signorini's law [8]. Here, $\lambda_N$ is the normal contact force and $g_N$ is the gap function. The subscripts $Ri$ and $Fi$ are temporarily removed for simplicity. This set-valued force law states that the contact is impenetrable, $g_N \geq 0$, the contact can only transmit pressure forces $\lambda_N \geq 0$ and the contact force $\lambda_N$ does not produce work $g_N \lambda_N = 0$. The force law can be expressed on different kinematic levels: displacement level (39), velocity level, and acceleration level. In the following we express all force laws for closed contact on velocity level, while all forces vanish for open contacts. Then, by employing concepts of convex analysis, the relationship between the relative velocity and the Lebesgue measurable normal contact force (not an impulse) may be written for a closed contact $g_N = 0$ as an inclusion on velocity level

$$-\gamma_N \in N_{C_N}(\lambda_N), \tag{40}$$

where the convex set $C_N = \{\lambda_N \mid \lambda_N \geq 0\} = \mathbb{R}^+$ is the set of admissible contact forces, and $N_{C_N}$ is the normal cone to $C_N$ [8]. The inclusion (40) is equivalent to the condition

$$\gamma_N \geq 0,\ \lambda_N \geq 0, \quad \gamma_N \lambda_N = 0, \tag{41}$$

for a closed contact $g_N = 0$. Before explaining the above force law (40), let us first mention that this force law describes the impenetrability of sustained contact, i.e. $g_N = 0$ and $\gamma_N = 0$, as well as detachment: $\gamma_N > 0 \Rightarrow \lambda_N = 0$. However, (40) does not cover impacts (where we have impulses instead of forces). For impacts we need a similar *impact law* described at the end of this subsection.

From the definition [8], [13] of a normal cone $N_C(\boldsymbol{x})$ to a convex set $C$ at the point $\boldsymbol{x} \in \mathbb{R}^n$, we have that $N_C(\boldsymbol{x}) = \{0\}$ for $\boldsymbol{x} \in \operatorname{int} C$, and $N_C(\boldsymbol{x}) = \{\emptyset\}$ for $\boldsymbol{x} \notin C$. If $\boldsymbol{x}$ is on the *boundary* of $C$, then $N_C(\boldsymbol{x})$ is the set of all vectors $\boldsymbol{y} \in \mathbb{R}^n$ that are normal to $\boldsymbol{x}$. For example, for $C_N = \mathbb{R}^+$ we have $N_{C_N}(0) = \mathbb{R}^-$.

The force law (40) only covers finite-valued contact efforts during impulse free motion, i.e. all velocities are absolutely continuous in time. When a collision occurs in a rigid-body setting, then the velocities will be locally discontinuous in order to prevent penetration. The velocity jump is accompanied by an impact impulse $P_N$, for which we will set up an impact law. The relative velocity admits, similarly to the velocities $\boldsymbol{u}$, a right $\gamma_N^+$ and a left $\gamma_N^-$ limit. The impact law for a completely inelastic impact at a closed contact can now be written as

$$-\gamma_N^+ \in N_{C_N}(P_N), \qquad C_N = \{P_N \mid P_N \geq 0\} = \mathbb{R}^+, \tag{42}$$

which is equivalent to the condition

$$\gamma_N^+ \geq 0,\ P_N \geq 0, \quad \gamma_N^+ P_N = 0. \tag{43}$$

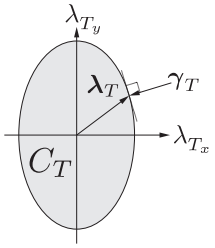


Fig. 3. Relationship between tangential relative velocity and friction force. The set $C_T$ is in grey.

*2) Coulomb Friction Force:* Similarly to the force law (40) for normal contact, we describe the constitutive description for friction using an inclusion on a normal cone. The friction force $\boldsymbol{\lambda}_T$, in the two-dimensional tangent plane to the contact point, is modeled with an anisotropic Coulomb friction law

$$-\boldsymbol{\gamma}_T \in N_{C_T}(\boldsymbol{\lambda}_T), \tag{44}$$

where $\boldsymbol{\gamma}_T$ is a relative sliding velocity, $N_{C_T}$ is the normal cone to the set $C_T$, and the ellipse

$$C_T = \left\{ \boldsymbol{\lambda}_T \ \middle|\ \frac{\lambda_{T_x}^2}{\left(\mu_{T_x}\lambda_N\right)^2} + \frac{\lambda_{T_y}^2}{\left(\mu_{T_y}\lambda_N\right)^2} \leq 1 \right\}, \tag{45}$$

is the set of admissible friction forces, where $\boldsymbol{\lambda}_T = \begin{bmatrix}\lambda_{T_x} & \lambda_{T_y}\end{bmatrix}^{\mathrm{T}}$, and $\mu_{T_x}$, $\mu_{T_y} > 0$ are directional friction coefficients along the $\boldsymbol{e}_x^{\Pi}$- and $\boldsymbol{e}_y^{\Pi}$-axis from (21), respectively. Fig. 3 depicts the set $C_T$ (in grey), together with the relationship between the tangential relative velocities and the friction force when it is on the boundary of $C_T$.

The force law (44) distinguishes between two cases: if the friction force is in the interior of $C_T$ or on its boundary. If $\boldsymbol{\lambda}_T \in \operatorname{int} C_T$, then it holds that $N_{C_T}(\boldsymbol{\lambda}_T) = \mathbf{0}$ from which we conclude that $\boldsymbol{\gamma}_T = \mathbf{0}$. Obviously, this corresponds to the stick phase of the friction law. If the friction force is on the boundary of $C_T$, then the normal cone $N_{C_T}(\boldsymbol{\lambda}_T)$ consists of the outward normal ray on the ellipse $C_T$ at the point $\boldsymbol{\lambda}_T$.

The advantage to formulate the friction law as the inclusion (44) now becomes apparent. First of all, note that (44), is a *spatial* friction law. Such a spatial friction law can not properly be described by a set-valued sign-function. Some authors [5], [14] model the spatial contact with two sign-functions for the two components of the relative sliding velocity using two friction coefficients $\mu_{T_x}$ and $\mu_{T_y}$. Others smoothen the (set-valued) sign function with a smoothening function, e.g. some arctangent function. This results in a very steep slope of the friction curve near zero relative velocity. Such an approach is very cumbersome for two reasons. First of all, stiction can not properly be described: an object on a slope will with a smoothened friction law always slide. Secondly, the very steep slope of the friction curve causes the differential equations of motion to become numerically stiff. Summarising, we see that (44) describes spatial Coulomb friction taking stiction properly into account.

*3) Constitutive Laws as Projections:* An inclusion can not be directly employed in numerical calculations. Hence, we transform the force laws (40) and (44), which have been stated as an inclusion to a normal cone, into an equality. This is achieved through the so-called proximal point function

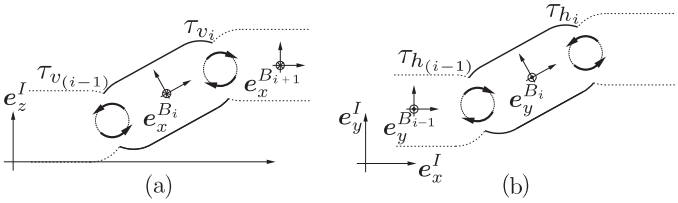


Fig. 4. Control Torques for (a) side-view and (b) top-view.

$\text{prox}_C(\boldsymbol{x})$, which equals $\boldsymbol{x}$ if $\boldsymbol{x} \in C$ and equals the closest point in $C$ to $\boldsymbol{x}$ if $\boldsymbol{x} \notin C$. The set $C$ must be convex. Using the proximal point function we transform the force laws into implicit equalities (see [8])

$$-\gamma_\kappa \in N_{C_\kappa}(\lambda_\kappa) \iff \lambda_\kappa = \text{prox}_{C_\kappa}\left(\lambda_\kappa - r_\kappa \gamma_\kappa\right), \quad (46)$$

where $r_\kappa > 0$ for $\kappa = N, T$.

### C. Joint Actuators

Each cardan joint has 2 DOF that are controlled by two joint actuators. The actuators are modeled as controlled torques applied around the axes of rotation for the joint. Fig. 4 illustrates how the direction of positive rotation is defined. Define a positive control torque $\tau_{v_i}$ to give a positive rotational velocity around $\boldsymbol{e}_x^{B_{i+1}}$ and a positive control torque $\tau_{h_i}$ to give a positive rotational velocity around $\boldsymbol{e}_y^{B_i}$, both with respect to link $i$. The total torque $\boldsymbol{\tau}_{C_i} \in \mathbb{R}^3$ applied to link $i$ is

$$\begin{aligned}\boldsymbol{\tau}_{C_i} = &\begin{bmatrix}0 & \tau_{h_i} & 0\end{bmatrix}^{\mathrm{T}} - \mathbf{R}_{B_{i-1}}^{B_i}\begin{bmatrix}0 & \tau_{h_{(i-1)}} & 0\end{bmatrix}^{\mathrm{T}} \\ &+ \mathbf{R}_{B_{i+1}}^{B_i}\begin{bmatrix}\tau_{v_i} & 0 & 0\end{bmatrix}^{\mathrm{T}} - \begin{bmatrix}\tau_{v_{(i-1)}} & 0 & 0\end{bmatrix}^{\mathrm{T}}\end{aligned} \quad (47)$$

for $i = 1, \ldots, n$, where the relative rotation matrix is

$$\mathbf{R}_{B_{i+1}}^{B_i} = \left(\mathbf{R}_{B_i}^{I}\right)^{\mathrm{T}} \mathbf{R}_{B_{i+1}}^{I}, \quad (48)$$

and $\tau_{h_0} = \tau_{v_0} = \tau_{h_n} = \tau_{v_n} = 0$. The vector of the torques applied to all links $\boldsymbol{\tau}_C \in \mathbb{R}^{6n}$ is

$$\boldsymbol{\tau}_C = \begin{bmatrix}\mathbf{0}_{1\times 3} & \boldsymbol{\tau}_{C_1}^{\mathrm{T}} & \mathbf{0}_{1\times 3} & \boldsymbol{\tau}_{C_2}^{\mathrm{T}} & \cdots & \mathbf{0}_{1\times 3} & \boldsymbol{\tau}_{C_n}^{\mathrm{T}}\end{bmatrix}^{\mathrm{T}}. \quad (49)$$

## V. Motion Pattern and Joint Control

In this chapter, we will define the joint angles and show how to control them for snake robot locomotion.

### A. Accessing and Control of Joint Angles

The joint angles are not directly accessible from the non-minimal coordinates, but can be calculated from the relative rotation matrices $\mathbf{R}_{B_{i+1}}^{B_i}$ in (48). Assume that $\mathbf{R}_{B_{i+1}}^{B_i}$ is constructed from successive rotations (Euler angles) $\alpha_{z_i}$, $\alpha_{h_i}$, and $\alpha_{v_i}$: $\mathbf{R}_{B_{i+1}}^{B_i} = \mathbf{R}_{\alpha_{zi}}\mathbf{R}_{\alpha_{hi}}\mathbf{R}_{\alpha_{vi}}$. Since we have cardan joints, let $\mathbf{R}_{\alpha_{zi}} = \mathbf{I}_{3\times 3}$ be the rotation around the $\boldsymbol{e}_z^{B_i}$-axis, and let $\mathbf{R}_{\alpha_{hi}}$ and $\mathbf{R}_{\alpha_{vi}}$ describe the rotation around $\boldsymbol{e}_y^{B_i}$ and $\boldsymbol{e}_x^{B_{i+1}}$, respectively. Hence, $\alpha_{h_i}$ describes the DOF of the cardan joint between link $i$ and link $i+1$ that moves link $i$ and $i+1$ from side to side, and $\alpha_{v_i}$ describes the lifting and lowering the links. The rotation angles can now be found from the relative rotation matrix as $\alpha_{v_i} = \tan^{-1}\left[(\mathbf{R}_{B_{i+1}}^{B_i})_{32}/(\mathbf{R}_{B_{i+1}}^{B_i})_{33}\right]$ and $\alpha_{h_i} = -\sin^{-1}(\mathbf{R}_{B_{i+1}}^{B_i})_{31}$, for $i = 1, \ldots, n-1$ where $\left(\mathbf{R}_{B_{i+1}}^{B_i}\right)_{32}$ is the element of $\mathbf{R}_{B_{i+1}}^{B_i}$ in row 3 column 2, etc.

Let the desired values of $\alpha_{h_i}$ and $\alpha_{v_i}$ be $\alpha_{h_i,r}$ and $\alpha_{v_i,r}$, respectively. Then, the proportional-derivative controllers (PD-control) for the joints are chosen to be

$$\tau_{h_i} = K_{h,p}\left(\alpha_{h_i} - \alpha_{h_i,r}\right) - K_{h,d}\left({}_{B_i}\boldsymbol{\omega}_{IB_i}\right)_2 \quad (50)$$

$$\tau_{v_i} = K_{v,p}\left(\alpha_{v_i} - \alpha_{v_i,r}\right) + K_{v,d}\left({}_{B_{i+1}}\boldsymbol{\omega}_{IB_{i+1}}\right)_1 \quad (51)$$

for $i = 1, \ldots, n-1$ where $K_{h,p}$, $K_{h,d}$, $K_{v,p}$, and $K_{v,d}$ are constants and equal for all $i$, and the subscripts $_2$ and $_1$ denote the second and first element of their respective vectors.

### B. Motion Pattern and Reference Angles

A general expression for defining some of the most used motion patterns is given by

$$\alpha_{h_i,r} = A_h \sin\left(\omega_h t + (i-1)\delta_h\right) + \psi_h \quad (52)$$

$$\alpha_{v_i,r} = A_v \sin\left(\omega_v t + (i-1)\delta_v + \delta_0\right) + \psi_v \quad (53)$$

for $i = 1, \ldots, n-1$ where $\alpha_{h_i,r}$ and $\alpha_{v_i,r}$ are the reference angles for $\alpha_{h_i}$ and $\alpha_{v_i}$, and $A_h$, $A_v$ are the amplitude of oscillation, $\omega_h$, $\omega_v$ are the angular frequencies, $\delta_h$, $\delta_v$ are the phase offsets, and $\psi_h$, $\psi_v$ are the angle offsets, for the horizontal and vertical wave, respectively [3]. The offset between the vertical and horizontal wave is given by $\delta_0$.

The motion pattern lateral undulation [1] is typical for biological and robot snakes and has been implemented in this paper. Snakes use this for locomotion by propagating horizontal waves from the front to the rear of the snake body while exploiting roughness in the terrain and digging its body into the ground. These latter two properties are the motivation for our anisotropic friction model.

## VI. Numerical Algorithm - Time-Stepping

The numerical solution of the equality of measures is found with an algorithm introduced in [11] (see also [8], [12]) called the time-stepping-method described in the following. Section VI-A and VI-B are based on [10], except for the novel direct calculation of the bilateral contact impulsions which we introduce.

### A. Time Discretization

Let $t_l$ denote the time at time-step $l = 1, 2, 3, \ldots$ where the step size is $\Delta t = t_{l+1} - t_l$. Consider the (usually very short) time interval $I = [t_A, t_E]$, and let $t_l = t_A$. Define $\boldsymbol{q}_A = \boldsymbol{q}(t_A)$, $\boldsymbol{u}_A = \boldsymbol{u}(t_A)$ which are admissible with respect to both the unilateral and bilateral constraints, and the unit norm constraint on the Euler parameters. Our goal is now to find $\boldsymbol{q}_E = \boldsymbol{q}(t_E)$. We use the states of the system at the *mid-point* $t_M = t_A + \frac{1}{2}\Delta t$ of the time-interval $I$ to decide which contact points are active (i.e. which links are touching the ground). The coordinates (positions and orientations) at $t_M$ are found from

$$\boldsymbol{q}_M = \boldsymbol{q}_A + \frac{\Delta t}{2}\mathbf{F}(\boldsymbol{q}_M)\boldsymbol{u}_A, \quad (54)$$

where we have used that $\dot{\boldsymbol{p}} = \frac{1}{2}\bar{\mathbf{H}}\,{}_{B_i}\boldsymbol{\omega}_{IB_i}$ [9],

$$\mathbf{F}(\boldsymbol{q}_M) = \begin{bmatrix}\mathbf{F}_{H_1} & \mathbf{0}_{7\times 6} & \cdots & \mathbf{0}_{7\times 6} \\ \mathbf{0}_{7\times 6} & \mathbf{F}_{H_2} & \cdots & \vdots \\ \vdots & & \ddots & \mathbf{0}_{7\times 6} \\ \mathbf{0}_{7\times 6} & \cdots & \mathbf{0}_{7\times 6} & \mathbf{F}_{H_n}\end{bmatrix} \quad (55)$$

$$\mathbf{F}_{H_i} = \begin{bmatrix}\mathbf{I}_{3\times 3} & \mathbf{0}_{4\times 3} \\ \mathbf{0}_{4\times 3} & \frac{1}{2}\bar{\mathbf{H}}_i^{\mathrm{T}}\end{bmatrix} \in \mathbb{R}^{7\times 6}, \quad (56)$$

and $\bar{\mathbf{H}}_i$ is found from (3) by inserting the orientation of link $i$ at time $t_M$. The approximation of the matrices $\mathbf{W}_\Xi$, where $\Xi = N, T, J$, on the time-interval $I$ is given as $\mathbf{W}_{\Xi M} := \mathbf{W}_\Xi(\boldsymbol{q}_M)$. The same applies for $\boldsymbol{h}_M := \boldsymbol{h}(\boldsymbol{q}_M, \boldsymbol{u}_A)$. A numerical approximation of the equality of measures (33) over the time-interval $I$ can now be written as

$$\mathbf{M}(\boldsymbol{u}_E - \boldsymbol{u}_A) - \boldsymbol{h}_M \Delta t - \boldsymbol{S} - \mathbf{W}_{JM}\boldsymbol{\Lambda}_J = \boldsymbol{\tau}_C \Delta t \quad (57)$$

where

$$\boldsymbol{S} = \sum_{a\in\mathcal{I}} (\mathbf{W}_{NM})_a \Lambda_{N_a} + [(\mathbf{W}_{TM})_{2a-1}\ (\mathbf{W}_{TM})_{2a}]\boldsymbol{\Lambda}_{T_a}, \quad (58)$$

and $\Lambda_{N_a}$, $\boldsymbol{\Lambda}_{T_a}$, and $\boldsymbol{\Lambda}_J$ are the contact impulsions during the time-interval $I$. They consist of forces $\lambda$ acting *during* $I$, and possible impulses $P$ acting *in* the time-interval $I$. To find the positions and orientations $\boldsymbol{q}_E$ at the end of the time-interval, we need to solve (57) for $\boldsymbol{u}_E$ and the contact impulsions. The contact impulsions associated with ground contact are found using the prox-functions described in Section IV-B.3 for the set of active contact points $\mathcal{I}$. Hence, the constitutive laws (46) for the ground contact impulsions may now be written

$$\Lambda_{N_a} = \text{prox}_{C_N}\left(\Lambda_{N_a} - r_N \gamma_{NE_a}\right), \quad (59)$$

$$\boldsymbol{\Lambda}_{T_a} = \text{prox}_{C_T}\left(\boldsymbol{\Lambda}_{T_a} - r_T \boldsymbol{\gamma}_{TE_a}\right), \quad (60)$$

where $r_N, r_T > 0,\ a \in \mathcal{I}$, $\gamma_{NE_a}$ is the $a$-th element of the vector $\boldsymbol{\gamma}_{NE}$, $\boldsymbol{\gamma}_{TE_a}$ is the vector of the $(2a-1)-$th and $2a$-th element of $\boldsymbol{\gamma}_{TE}$, and

$$\boldsymbol{\gamma}_{NE} := \boldsymbol{\gamma}_N(\boldsymbol{q}_M, \boldsymbol{u}_E) = \mathbf{W}_{NM}^{\mathrm{T}}\boldsymbol{u}_E, \quad (61)$$

$$\boldsymbol{\gamma}_{TE} := \boldsymbol{\gamma}_T(\boldsymbol{q}_M, \boldsymbol{u}_E) = \mathbf{W}_{TM}^{\mathrm{T}}\boldsymbol{u}_E. \quad (62)$$

The constitutive laws (59)-(62) are valid for completely inelastic impact.

The constraints on the joints are bilateral and it therefore holds that $\boldsymbol{\gamma}_{JE} := \boldsymbol{\gamma}_J(\boldsymbol{q}_E, \boldsymbol{u}_E) = \mathbf{W}_{JM}^{\mathrm{T}}\boldsymbol{u}_E = \mathbf{0}\,\forall t$. This allows us to directly compute the associated contact impulsions $\boldsymbol{\Lambda}_J$ by solving (57) for $\boldsymbol{\Lambda}_J$ with $\boldsymbol{u}_E = \mathbf{0}$. By solving for $\boldsymbol{\Lambda}_J$ and solving (57)-(62), we find that

$$\boldsymbol{q}_E = \boldsymbol{q}_M + \frac{\Delta t}{2}\mathbf{F}(\boldsymbol{q}_M)\boldsymbol{u}_E. \quad (63)$$

### *B. Solving for the Contact Impulsions*

The numerical integration algorithm used in this paper is called a time-stepping method which allows for a simultaneous treatment of both impulsive and non-impulsive forces during a time-step. The frictional contact problem, defined by (57)-(62) and finding $\boldsymbol{\Lambda}_J$, needs to be solved for each time-step $t_l$. A Modified Newton Algorithm [15] has been chosen to solve the nonlinear problem iteratively because of its simplicity. Let the superscript $^{(k)}$ denote the current iteration of the Modified Newton Algorithm, and initialize all contact impulses that were not active in the previous time-step $t_{l-1}$ with zero. Let those that *were* active be initialized with their previous values. Now, the algorithm may be written as

1) Solve

$$\boldsymbol{\Lambda}_J^{(k)} = \left(\mathbf{W}_J^{\mathrm{T}}\mathbf{M}^{-1}\mathbf{W}_J^{-1}\right)^{-1} \cdot \left[\mathbf{W}_J^{\mathrm{T}}\boldsymbol{u}_A - \mathbf{W}_{JM}^{\mathrm{T}}\mathbf{M}^{-1}\left(\boldsymbol{h}_M\Delta t + \boldsymbol{S}^{(k)}\right)\right] \quad (64)$$

where

$$\boldsymbol{S}^{(k)} = \sum_{a\in\mathcal{I}} (\mathbf{W}_{NM})_a\, \Lambda_{N_a}^{(k)} + \sum_{a\in\mathcal{I}} [(\mathbf{W}_{TM})_{2a-1}\ (\mathbf{W}_{TM})_{2a}]\ \boldsymbol{\Lambda}_{T_a}^{(k)}. \quad (65)$$

2) Solve $\boldsymbol{u}_E^{(k+1)}$ from

$$\mathbf{M}\left(\boldsymbol{u}_E^{(k+1)} - \boldsymbol{u}_A\right) - \boldsymbol{h}_M\Delta t - \boldsymbol{S}^{(k)} - \mathbf{W}_{JM}\boldsymbol{\Lambda}_J^{(k)} = \boldsymbol{\tau}_C\Delta t \quad (66)$$

3) Solve for $a \in \mathcal{I}$

$$\Lambda_{N_a}^{(k+1)} = \text{prox}_{C_N}\left(\Lambda_{N_a}^{(k)} - r_N\gamma_{NE_a}^{(k+1)}\right) \quad (67)$$

$$\boldsymbol{\Lambda}_{T_a}^{(k+1)} = \text{prox}_{C_T}\left(\boldsymbol{\Lambda}_{T_a}^{(k)} - r_T\boldsymbol{\gamma}_{TE_a}^{(k+1)}\right) \quad (68)$$

where

$$\boldsymbol{\gamma}_{NE}^{(k+1)} = \mathbf{W}_{NM}^{\mathrm{T}}\boldsymbol{u}_E^{(k+1)}, \quad \boldsymbol{\gamma}_{TE}^{(k+1)} = \mathbf{W}_{TM}^{\mathrm{T}}\boldsymbol{u}_E^{(k+1)} \quad (69)$$

Repeat steps 1. to 3. until

$$\|\boldsymbol{\Lambda}_N^{(k+1)} - \boldsymbol{\Lambda}_N^{(k)}\| + \|\boldsymbol{\Lambda}_T^{(k+1)} - \boldsymbol{\Lambda}_T^{(k)}\| < \epsilon, \quad (70)$$

where $\epsilon > 0$ is a user-defined tolerance. Subsequently, $\boldsymbol{q}_E$ is calculated from (63) and the calculation of the time-step is finished. Usually, a higher value of the parameters $r_N$, $r_T$ yields a faster convergence rate at the risk of divergence. However, a general convergence result for the Modified Newton Algorithm does not exist. The constitutive laws (67)-(69) used to describe the contact impulses are given on *velocity level*. This means that the unilateral and bilateral constraints on position level, and the unit norm constraint on the Euler parameters are in general not satisfied. A solution to these problems is suggested in the following.

### *C. Constraint Violation*

After the Modified Newton Algorithm has converged and $\boldsymbol{q}_E$ has been found from (63), the unit-norm constraint $\|\boldsymbol{p}_i\| = 1$ is satisfied from $\boldsymbol{p}_{E_i}^{new} = \boldsymbol{p}_{E_i}/\|\boldsymbol{p}_{E_i}\|$ for $i = 1, \ldots, n$ where $\boldsymbol{p}_{E_i}$ is the quaternion describing the orientation of link $i$. The new quaternions should now be inserted into $\boldsymbol{q}_E$.

The links have to be projected so that the bilateral constraints (8), (9) are satisfied. This is done in a two-step process while keeping the position and orientation of link 1 fixed. First, the orientation of the remaining links are altered so that $g_{Ji_\phi} = 0$ is satisfied for $i = 1, \ldots, n-1$. In this process, all the $\boldsymbol{e}_{\tilde{z}}^{B_i}$-axes are kept fixed, while the $\boldsymbol{e}_x^{B_i}$ and $\boldsymbol{e}_y^{B_i}$ are changed if necessary. Subsequently, the remaining links are translated so that $g_{Ji_\chi} = 0$ is satisfied for $i = 1, \ldots, n-1$, $\chi = x, y, z$. The new positions of the links should now be inserted into $\boldsymbol{q}_E$.

## VII. Numerical Results

In this section we will demonstrate the robustness of the numerical implementation by letting the snake drop to the floor from an inclined angle, and then move the snake robot across the floor by the motion pattern called lateral undulation.

The choice of parameters used to describe the snake robot is based on the water-hydraulic based snake robot built by the Norwegian research organisation Sintef in Trondheim [16]. The model parameters are for $i = 1, \ldots, n$: $n = 11$ links,

$L_i = 0.269$ m, $L_{SC} = 0.0795$ m, $L_{GS_i} = 0.1016$ m, $m_i = 7$ kg, $\Theta_{1i} = 0.0450\,\mathrm{kg\,m^2}$, $\Theta_{3i} = 0.0055\,\mathrm{kg\,m^2}$, and the PD-controller is implemented with the gains $K_{h,p} = 400$ Nm, $K_{h,d} = 20$ Nm, $K_{v,p} = 200$ Nm, and $K_{v,d} = 10$ Nm. The simulation parameters are $r_N = 2$, $r_T = 0.5$, and $\Delta t = \frac{t_{\text{stop}} - t_{\text{start}}}{N-1}$, where $N$ is the number of integration steps, and $t_{\text{start}}$ and $t_{\text{stop}}$ is the start and stop time of the simulation, respectively. Frictional coefficients are $\mu_{T_x} = 0.01$ and $\mu_{T_y} = 0.05$.

### A. Floor Impact

The snake robot is dropped at an inclined angle of 30 degrees with respect to the floor. The lowest link is lifted to $z_1 = 0.38$ m above the floor. Fig. 5 shows the configuration of the snake robot while it drops to the floor with all the joint controllers turned off. Fig. 6 depicts (a) the vertical position

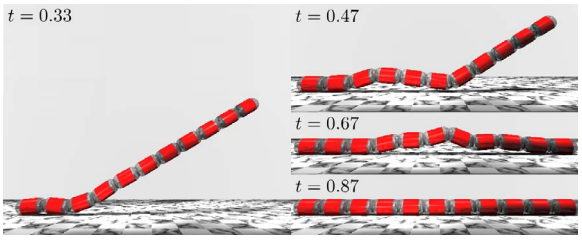


Fig. 5. Snake robot during drop and impact.

$z_1$ of link 1 and (b) its drop velocity $u_{z1}$ (parallel to the $\boldsymbol{e}_z^I$-axis). As seen in (b), velocity jumps occur during the impacts with the ground.

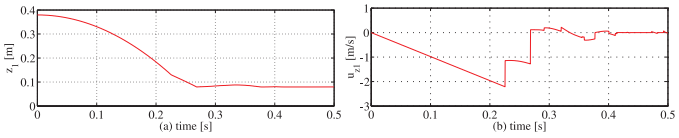


Fig. 6. Vertical (a) position and (b) velocity of link 1 during drop and impact.

### B. Lateral Undulation as Motion Pattern

The reference angles for the joints are found from (52)-(53) with $A_h = 30\pi/180$, $\omega_h = 135\pi/180\ \frac{1}{s}$, $\delta_h = -50\pi/180$, and $A_v = \omega_v = \delta_v = \psi_v = 0$. We see from Fig. 7 that even though the snake robot started from a non-idealized posture (after the drop), the numerical treatment was stable. The snake

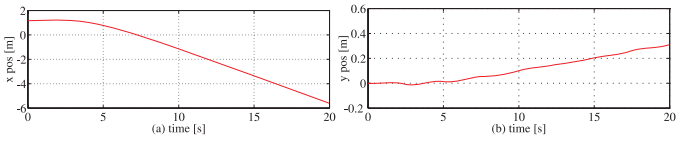


Fig. 7. Position of the centre of gravity of the snake robot along the (a) $\boldsymbol{e}_x^I$-axis and (b) $\boldsymbol{e}_y^I$-axis.

robot would not have been able to move forward with this motion pattern on the flat ground if it had not been for the orthotropic friction model.

## VIII. Conclusions and Further Work

A 3D mathematical model based on the framework of non-smooth dynamics and convex analysis has been presented. It is shown how to easily incorporate the effect of contact and friction forces by set-valued force laws.

The use of the non-minimal absolute coordinates resulted in a constant mass matrix and an effective way of writing the system equations. It was possible to include the control torques in the model without referring to the inertial frame even though all positions and orientations are given in this frame. Also, total simulation time is decreased since it is not necessary to calculate a new mass matrix for every iteration of the Modified Newton Algorithm.

As opposed to the other contact and friction forces, the bilateral constraint forces in the joints have been calculated directly from the equality of measures without using the prox-function. This resulted in a much more stable numerical treatment.

Suggestions to further work are: 1) extend the model to other ground shapes than a flat floor, and 2) include the possibility for snake robot locomotion using obstacles.

It is hoped that this paper can inspire other communities working on robot manipulators to try out the powerful modeling techniques available in the framework of non-smooth dynamics and convex analysis.

## References


[1] S. Hirose, *Biologically Inspired Robots: Snake-Like Locomotors and Manipulators*. Oxford: Oxford University Press, 1993.

[2] S. Ma, Y. Ohmameuda, and K. Inoue, "Dynamic analysis of 3-dimensional snake robots," in *Proc. IEEE/RSJ Int. Conf. On Intelligent Robots and Systems*, 2004, pp. 767–772.

[3] P. Liljebäck, Ø. Stavdahl, and K. Y. Pettersen, "Modular pneumatic snake robot: 3D modelling, implementation and control," in *Proc. 16th IFAC World Congress*, July 2005.

[4] K. McIsaac and J. Ostrowski, "Motion planning for anguilliform locomotion," *IEEE Trans. Robot. Autom.*, vol. 19, no. 4, pp. 637–625, August 2003.

[5] M. Saito, M. Fukaya, and T. Iwasaki, "Serpentine locomotion with robotic snakes," *IEEE Contr. Syst. Mag.*, vol. 22, no. 1, pp. 64–81, February 2002.

[6] B. Brogliato, *Nonsmooth Mechanics*, 2nd ed. London: Springer, 1999.

[7] Ch. Glocker, *Set-Valued Force Laws, Dynamics of Non-Smooth Systems*, ser. Lecture Notes in Applied Mechanics. Berlin: Springer-Verlag, 2001, vol. 1.

[8] R. I. Leine and H. Nijmeijer, *Dynamics and Bifurcations of Non-Smooth Mechanical Systems*, ser. Lecture Notes in Applied and Computational Mechanics. Berlin: Springer Verlag, 2004, vol. 18.

[9] O. Egeland and J. T. Gravdahl, *Modeling and Simulation for Automatic Control*. Trondheim, Norway: Marine Cybernetics, 2002.

[10] C. Le Saux, R. I. Leine, and Ch. Glocker, "Dynamics of a rolling disk in the presence of dry friction," *Journal of Nonlinear Science*, vol. 15, no. 1, pp. 27–61, 2005.

[11] J. J. Moreau, "Unilateral contact and dry friction in finite freedom dynamics," in *Non-Smooth Mechanics and Applications*, ser. CISM Courses and Lectures, J. J. Moreau and P. D. Panagiotopoulos, Eds. Wien: Springer Verlag, 1988, vol. 302, pp. 1–82.

[12] Ch. Glocker and C. Studer, "Formulation and preparation for numerical evaluation of linear complementarity systems in dynamics," *Multibody System Dynamics*, vol. 13, pp. 447–463, 2005.

[13] R. T. Rockafellar, *Convex Analysis*, ser. Princeton Landmarks in Mathematics. Princeton, New Jersey: Princeton University Press, 1970.

[14] S. Ma, N. Tadokoro, B. Li, and K. Inoue, "Analysis of creeping locomotion of a snake robot on a slope," in *Proc. IEEE Int. Conf. Robotics and Automation*, September 2003, pp. 2073–2078.

[15] P. Alart and A. Curnier, "A mixed formulation for frictional contact problems prone to Newton like solution methods," *Comput. Method. Appl. M.*, vol. 92, pp. 353–375, 1991.

[16] P. Liljebäck, Ø. Stavdahl, and A. Beitnes, "SnakeFighter. development of a water hydraulic fire fighting snake robot," in *Proc. IEEE Int. Conf. Control, Automation, Robotics, and Vision*, Dec 2006.